# Evidence of pervasive trans-tensional deformation in the northwestern Wharton Basin in the 2012 earthquakes rupture area

Nugroho Hananto, Asmoune Boudarine, Hélène Carton, Satish C Singh, Praditya Avianto, Jerome Dyment, Yanfang Qin, Dibakar Ghosal, Rina Zuraida, Paul Tapponnier, et al.

Earth and Planetary Science Letters 502 (2018) 174–186

Contents lists available at ScienceDirect

Earth and Planetary Science Letters

www.elsevier.com/locate/epsl

# Evidence of pervasive trans-tensional deformation in the northwestern Wharton Basin in the 2012 earthquakes rupture area

Nugroho Hananto [a], Asmoune Boudarine [b], Hélène Carton [b], Satish C. Singh [b,e,*], Praditya Avianto [a], Jérôme Dyment [b], Yanfang Qin [b], Dibakar Ghosal [c], Rina Zuraida [d], Paul E. Tapponnier [e], Christine Deplus [b], Kerry Sieh [e]

[a] Research Center for Oceanography, Indonesian Institute of Sciences, Jl Pasir Putih 1 Ancol Timur, Jakarta Utara 14430, Indonesia
[b] Equipe de Géosciences Marines, Institut de Physique du Globe de Paris (CNRS, Paris Diderot, Sorbonne Paris Cité), 1 rue Jussieu, 75238 Paris Cedex 05, France
[c] Indian Institute of Technology, Kanpur, India
[d] Marine Geological Institute, Jl DR. Junjunan 236, Bandung, Indonesia
[e] Earth Observatory of Singapore, Nanyang Technological University, N2-01A-XX, 50 Nanyang Avenue, Singapore 639798, Singapore

ARTICLE INFO

*Article history:*
Received 26 November 2017
Received in revised form 31 August 2018
Accepted 5 September 2018
Available online 18 September 2018
Editor: J.-P. Avouac

*Keywords:*
the 2012 Indian Ocean earthquake
diffuse deformation
Wharton Basin
plate bending
shear zones
normal faults

ABSTRACT

The Wharton Basin in the Indian Ocean is one of the most extensively deforming ocean basins, as confirmed by the occurrence of several very large earthquakes starting from January 12, 2012 with Mw 7.2 followed by the great earthquakes of April 11, 2012 with Mw 8.6 and Mw 8.2. Although the Mw 7.2 and Mw 8.2 earthquakes seem to have ruptured the re-activated N–S striking fracture zones, the largest event (Mw 8.6) required the rupturing of several faults, oblique to each other, in a very complex manner. In order to understand the nature of deformation in these earthquakes rupture zones, we recently acquired 90 000 km$^2$ of bathymetry, 11 400 km of sub-bottom profiling, gravity and magnetic data covering the rupture areas of the 2012 earthquakes east of the Ninety-East Ridge, in the northwestern Wharton Basin. These new data reveal six N8°E striking re-activated fracture zones (F5b, F6a, f6b, F7a, F7b and F8), where the fracture zone F6a can be followed for over 400 km and seems to be most active. The epicenters of the Mw 8.6 and Mw 8.2 earthquakes lie on the fracture zones F6a and F7b, respectively. The newly observed fracture F5b in the east is short, and has an extensional basin at its southern tip. The fracture zone F8 defines the eastern boundary of the Ninety-East Ridge. The presence of en echelon faults and pull-apart basins indicate left-lateral motion along these fracture zones. In between these fracture zones, we observe pervasive 290° striking right-lateral shear zones at 4–8 km intervals; one of which has cut through a seamount that might have ruptured during the Mw 8.6 earthquake. We also observe another N20°E striking left-lateral shear zones in the vicinity of F7b and F8, which is coincident with the strike of one of the nodal planes of the Mw 8.6 focal mechanism. These N20°E striking shear zones are interpreted as R Riedel shears and the N290°E striking shear zones as R′ Riedel shears. These shear zones are formed by a series of N335°E striking en echelon normal faults. Our data also show the presence of N65°E striking thrust faults east of the Ninety-East Ridge, orthogonal to the regional principal direction of compression. Furthermore, extensive bending-related faulting is also observed close to the Sumatra trench with normal faults also striking at N335°E, similar to the normal faults that form the shear zones. Normal faults with a similar orientation are also present at the southern tip of F5b. We explain all these observations with a single coherent model of deformation in the Wharton Basin, where a dominant part of the regional NW–SE compressional stress is accommodated along the N8°E re-activated fracture zones, and the rest is distributed along shear zones, thrust and normal faults between these fracture zones. The thrust and normal faults are orthogonal to each other and define the direction of principal compressive and extensive stresses in the region whereas the two shear zone systems form a conjugate pair.



## 1. Introduction

The largest recorded intra-plate oceanic strike-slip earthquake of Mw 8.6 occurred on April 11, 2012 in the Wharton Basin with its epicenter about 120 km southwest of the Sunda trench. It was

* Corresponding author at: Equipe de Géosciences Marines, Institut de Physique du Globe de Paris (CNRS, Paris Diderot, Sorbonne Paris Cité), 1 rue Jussieu, 75238 Paris Cedex 05, France.
*E-mail address:* singh@ipgp.fr (S.C. Singh).

https://doi.org/10.1016/j.epsl.2018.09.007

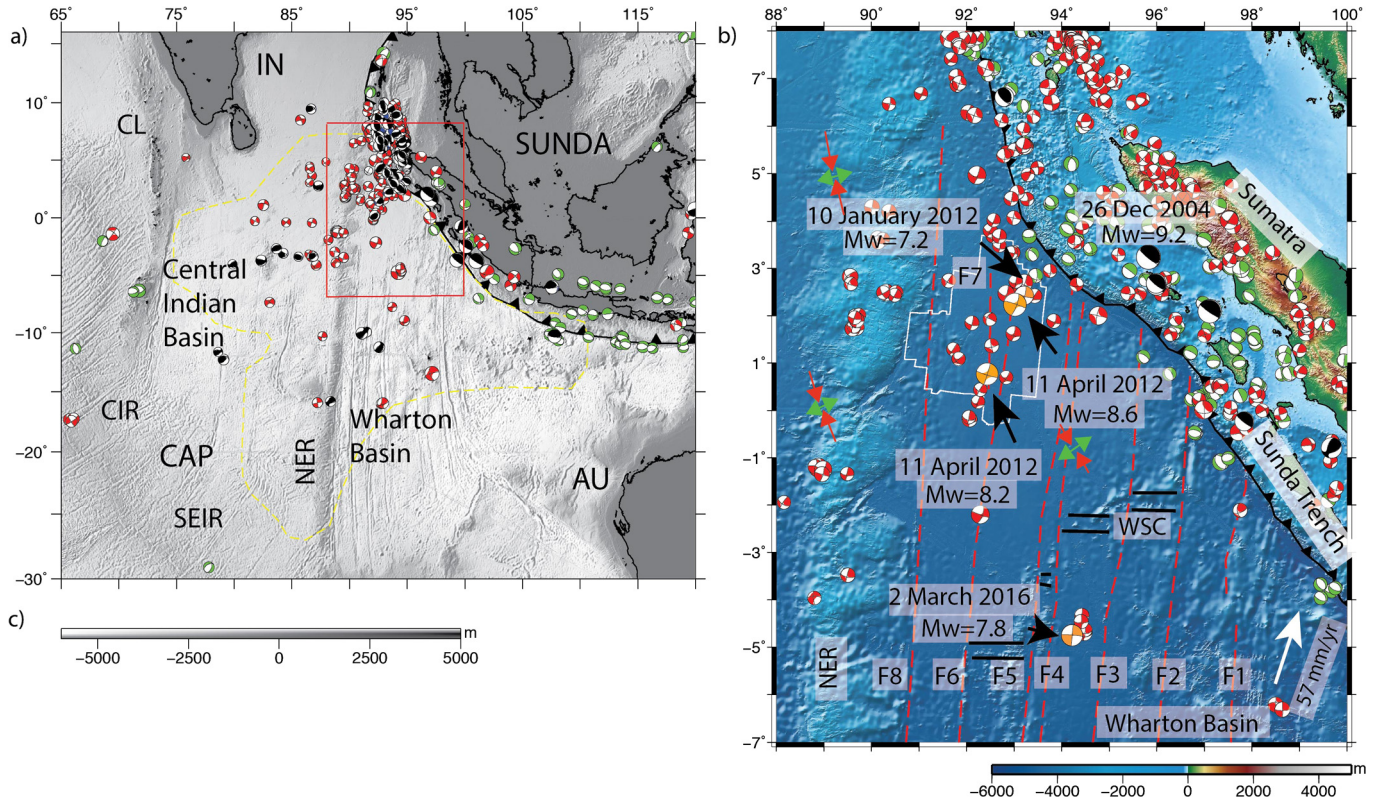


**Fig. 1.** (a) Regional tectonic setting of the composite Indo-Australian plate. Dashed yellow lines define the diffuse plate boundaries between IN (India), AU (Australia) and CAP (Capricorn) plates (after Royer and Gordon, 1997). Red box shows location of figure (b). CL = Chagos–Laccadive Ridge; CIR = Central Indian Ridge; SEIR = Southeast Indian Ridge; NER = Ninety-East Ridge. Seafloor topography is from ETOPO1 (Amante and Eakins, 2009). The beach balls indicate normal (green), thrust (black) and strike-slip (red) earthquakes. All the beach balls are plotted with their circle radii proportional to magnitude. (b) Oceanic plate structure in the Wharton Basin. Fracture zones (red dashed lines) and fossil Wharton Spreading Centre (double black line) are from Singh et al. (2011) identified from altimetry data. White arrows mark the convergence direction of the Indo-Australian Plate with respect to the Sunda Plate (Prawirodirdjo et al., 2000). Beach balls show historical seismicity recorded in the Wharton Basin since 2010. Focal mechanisms represent all magnitudes >5 Global CMT solutions (Ekström et al., 2012) from January 2010 to May 2017. Only Mw > 7.8 thrust earthquakes in the subduction zone are shown. The combined red–green arrows indicate the directions and the relative magnitudes of the principal deviatoric compression and tension components of stress (Gordon and Houseman, 2015). The three orange beach balls indicate the Mw 8.6 main shock and its Mw 8.2 aftershock, and Mw 7.2 foreshock. The 2nd March 2016 Mw 7.8 earthquake is also marked. The white line delimits the newly acquired bathymetric data shown in Fig. 3. (For interpretation of the colors in the figure(s), the reader is referred to the web version of this article.)

preceded by a foreshock of Mw = 7.2 on January 10, 2012 and followed by an aftershock of Mw = 8.2 two hours later (Duputel et al., 2012), along with hundreds of smaller aftershocks (Figs. 1, 2). It has been suggested that this earthquake occurred as a result of stress transfer on the incoming plate after the 2004 Mw 9.2 Sumatra–Andaman earthquake and the 2005 Mw 8.7 Nias earthquake (Delescluse et al., 2012).

This part of the Wharton Basin lies in a broad deformation zone within the composite Indo-Australian plate, extending from the Chagos–Laccadive ridge in the west to the Investigator Ridge in the east (Royer and Gordon, 1997) (Fig. 1a). Although this region is well known for distributed deformation within an oceanic plate (Gordon, 2000), many details about its seafloor morphology and tectonic activity are lacking, owing to its large extent and remote location. GPS and marine geophysical studies indicate that compressional faults and folds occur west of the Ninety-East Ridge (NER) in the Central Indian Basin south of India (Bull and Scrutton, 1990; Delescluse and Chamot-Rooke, 2007). In contrast, deformation is mainly accommodated by strike-slip faulting along re-activated N–S striking fracture zones in the Wharton Basin to the east of the NER (Deplus et al., 1998; Deplus, 2001) (Fig. 1b).

The occurrence of such a large earthquake with a high stress drop away from major plate boundaries came as a surprise (McGuire and Beroza, 2012). Although the foreshock and the main aftershock seem to have ruptured along re-activated fracture zones, the main event (Mw 8.6) appears to have ruptured several faults, oblique to one another, in a very complex manner (Hill et al., 2015; Wei et al., 2013; Ishii et al., 2013; Meng et al., 2012; Yue et al., 2012) (Fig. 2). This suggests that deformation in the northern Wharton Basin is distributed over a number of faults, but the exact geometry of this fault system and the identification of the main structures are still open questions. Most models based on seismological and geodetic studies agree that the Mw 8.6 main shock involved rupture on one NNE–SSW trending fault along with at least one WNW–ESE trending fault, with the seismic moment released dominantly during the NNE–SSW rupture. The limited existing bathymetry data show recent activity along these fracture zones (Deplus et al., 1998; Graindorge et al., 2008) but their strike is no more than 8°E (Carton et al., 2014; Singh et al., 2017). On the other hand, the GCMT solution for the main event shows one nodal plane striking 20°E, and none of the fault geometries associated with models of coseismic slip distribution align with the existing fracture zones (Fig. 2). Based on limited bathymetry (75 km by 100 km) and high-resolution seismic reflection data in the vicinity of the Mw 8.2 aftershock, Singh et al. (2017) found the existence of N294°E trending shear zones in addition to the N–S re-activated fracture zones, and suggested that these two fault systems form a conjugate pair of faults, accommodating the large-scale deformation observed in the Wharton Basin. However, the 2012 Mw 8.6 earthquake rupture extends over a very large area that is very poorly sampled by marine geophysical data, leading to major uncertainties regarding the exact location and geometry of faults activated during this earthquake.

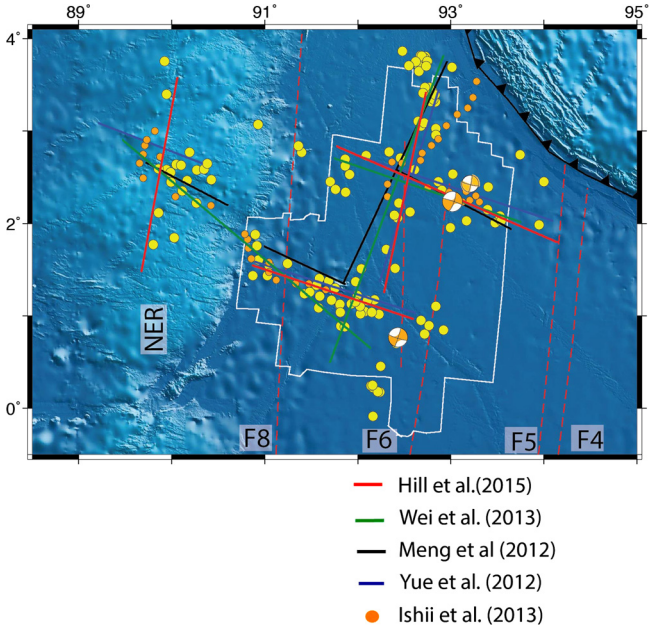


**Fig. 2.** 2012 Wharton Basin earthquake sequence (orange beach balls). The epicenters for the first 4 days of the 2012 aftershock sequence are shown with yellow dots (USGS catalog). The colored lines indicate five models of coseismic slip distribution of the Mw 8.6 earthquake (Hill et al., 2015; Wei et al., 2013; Ishii et al., 2013; Meng et al., 2012; Yue et al., 2012). The red dashed lines indicate fracture zones F4 to F8. NER: Ninety-East Ridge.

In July 2016, we acquired ~90 000 km$^2$ of high-resolution multibeam bathymetry, 11 400 km of 3.5 kHz echo-sounder, gravity and magnetic data on board the French Research Vessel Marion Dufresne, during the MIRAGE (Marine Investigation of the Rupture Anatomy of the 2012 Great Earthquake) experiment covering the 2012 earthquakes rupture areas in the Wharton Basin. Here we present the first detailed investigation of the seafloor morphology and its relations with the Mw 8.6 earthquake rupture, and provide a comprehensive model of active deformation in the Wharton Basin.

## 2. Tectonic setting

The NE Indian Ocean is a complex region with a rich tectonic history initiated during the breakup of India and Australia at ~155 Ma (Sager et al., 1992; Heine and Müller, 2005). The spreading between India and Australia was initially taking place along a NW–SE direction, creating the western Australian basin. It re-oriented along an E–W direction at ~100 Ma, forming the major N–S oriented fracture zones observed in the Wharton Basin. The spreading velocity was fast prior to the collision of India with Eurasia, with India moving at ~8–10 cm/yr at ~70 Ma, and abruptly slowing down to 2–4 cm/yr at ~40 Ma (Molnar and Tapponnier, 1977), while the spreading at the Wharton Spreading Centre ceased between 38 Ma and 36.5 Ma (Jacob et al., 2014). Following this cessation, India and Australia became a single rigid plate (Liu et al., 1983).

Royer and Gordon (1997) suggested that the Indo-Australian plate can be considered a composite plate system with three component plates (India, Australia and Capricorn; Fig. 1) bounded by diffuse boundary regions. Deformation within the Indian Ocean extends from the Central Indian Basin across the NER to the northwest shelf of Australia (Fig. 1a) (Weissel et al., 1980; Petroy and Wiens, 1989; Wiens and Stein, 1984). The northern side of the composite Indo-Australian plate displays a change in boundary conditions from west to east, with continental collision of India with Eurasia, oblique subduction at the Sumatra trench and frontal subduction along the Java Trench. This is accompanied by the rotation of the principal compressional stress direction, which is oriented N–S west of the NER in the Central Indian Basin, explaining the formation of folds and E–W oriented reverse faults in this area (Bull and Scrutton, 1992), and NW–SE east of the NER in the Wharton Basin (Fig. 1b), where left lateral strike-slip faulting is prevalent along N–S trending re-activated fracture zones (Deplus et al., 1998). Therefore, the NER has been suggested to act as a natural mechanical barrier separating two different deformation patterns (Delescluse and Chamot-Rooke, 2007; Sager et al., 2013). However, the recent regional stress field computation (Gordon and Houseman, 2015) indicates that the change in the direction of maximum compressive stress is more gradual from N10°W at 5°N at the NER, increasing to N20°W at the equator and N30°W further east at 95°E (Fig. 1b).

Our study area lies within the northern Wharton Basin, which is bounded by the Sunda Trench in the north, the NER in the west and the fossil Wharton Spreading Centre in the south (Fig. 1b). The sediment thickness in the southern part of the study area is about 2.2 km (Singh et al., 2017). Closer to the Sunda trench, offshore north Sumatra, the sediment thickness ranges between 2.5 and 4 km (Moeremans et al., 2014). This sediment thickness reflects the >200 meters per million years Nicobar fan deposition that began ~9.5 million years ago (Hüpers et al., 2017).

The Indian Ocean within its equatorial band displays a higher seismicity rate than any other ocean basin (Fig. 1b), particularly after the 2004 Sumatra–Andaman earthquake (Wiseman and Bürgmann, 2012). Seismicity in the Wharton Basin and on the NER is dominated by strike-slip solutions (Fig. 1b), with a component of thrusting in some cases. Active deformation within the Wharton Basin had long been detected but its true intensity was revealed through the 2012 earthquake sequences and more recently by the Mw 7.8 strike-slip earthquake on March 2, 2016 (Lay et al., 2016) further south (Fig. 1b), and which makes it a unique site to study intra-oceanic earthquakes and associated deformation.

## 3. Results

The high-resolution multibeam data were acquired using the EM 122 Multibeam Echo Sounder providing 5–10 m vertical and 25–50 m lateral resolutions and the sub-bottom 3.5 kHz profiles using a Kongsberg SBP 120 system. The data were acquired at N5°E azimuth, parallel to the azimuth of the fracture zones, with length varying from 100 to 400 km. Fig. S1 shows the location of profiles. The earthquake locations were taken from National Earthquake Information Center (NEIC) (http://earthquake.usgs.gov/earthquakes/eqarchives/epic) and the fault plane solution from the Global Centroid Moment Tensor (GCMT) (http://www.globalcmt.org/CMTsearch.html).

### 3.1. General morphology

Both un-interpreted and interpreted multibeam bathymetry image covering a region of roughly 4.5° × 3.5° are shown in Fig. 3. Seafloor is relatively flat (4500 m), except near the NER and a seamount discovered east of the NER. The main seamount rises to 2600 m, and is elongated in ENE direction. Near the subduction front, the trench is characterized by a bathymetry low, ranging from 4500 m in the northwest to 4700 m in the northeast. At about 100 km from the trench, one can clearly see a NW–SE trending 200 km wide outer rise bulge region, associated with the bending and flexure of the downgoing oceanic lithosphere, punctuated by subsidence around the re-activated N–S fracture zones and shear zones. The flexural bend is clearly visible on the 3.5 kHz profile (Fig. 3c), which also shows extensive faulting. The second most prominent features are pervasive 290° striking shear zones

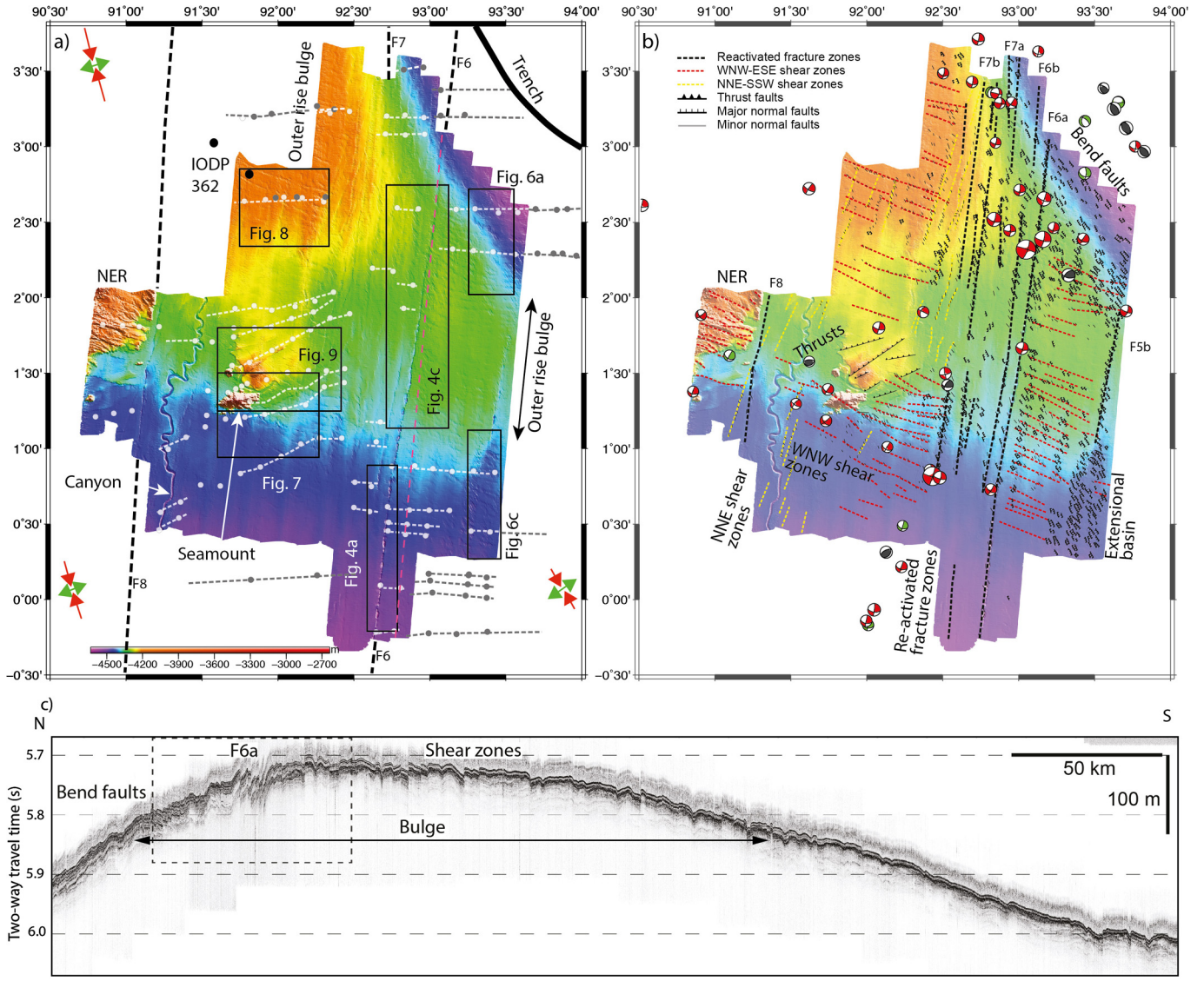


**Fig. 3.** (a) Bathymetry map (shaded relief with illumination from the NE) of the Wharton Basin, acquired during the MIRAGE 1 cruise. Black boxes show location of figures detailed in the following sections. The thick black dashed lines indicate reactivated fracture zones F6 to F8 outside of our study area. White dots are magnetic anomaly picks and the white dashed lines represent magnetic lineations. Grey dots and dashed grey lines indicate the magnetic anomaly from Jacob et al. (2014). Small black circles represent location of the IODP Leg 362 boreholes. The combined red–green arrows indicate the directions and the relative magnitudes of the principal deviatoric compression and tension components of stress (Gordon and Houseman, 2015). Pink dashed line indicates the location of 3.5 kHz profile shown in figure c. (b) Interpreted bathymetry showing N–S re-activated fracture zones (black dashed lines), WNW–ESE shear zones (red dashed lines), NNE–SSW shear zones (yellow dashed lines), thrusts and normal faults (black). Beach balls show historical seismicity recorded in the Wharton Basin since 2010. Focal mechanisms represent all magnitudes >5 Global CMT solutions (Ekström et al., 2012) from January 2010 to May 2017. (c) 3.5 kHz echo-sounder North–South profile 5 (see also Fig. S1 for the location) showing the flexural bulge, intense faulting around F6a, bend faults near the trench, and shear zones. Seafloor is marked in light blue and a sedimentary layer in yellow.

between the re-activated fracture zones. We have also discovered new N20°E striking shear zones between the fracture zones and the NER.

The northeastern part of the study area gently dips toward the trench and is marked by a series of sub-parallel graben features, oriented roughly parallel to the trench direction, related to bend faulting. A relative bathymetric high is observed in the region north of the seamount, which is due to thrust faulting (discussed below). Toward the southeast domain, a large bathymetric low is easily distinguishable, forming an extensional basin.

Several north–south oriented channels are present in the whole study area; the most prominent channel is located just east of the NER (Fig. 3a), flowing southward and can be observed over 170 km in our image but could be traced further north for about 100 km on previous bathymetry. The origin of this channel is difficult to decipher as it lies between the NER and the trench (see also Geersen et al., 2015). There are two other abandoned channels further east, suggesting a westward migration of these channels.

In the following sections, we will discuss the main tectonic features observed in our study:

### 3.2. Reactivated fracture zones

The new bathymetry data reveal eight N–S trending re-activated fracture zones (Fig. 3), F5b, F6a, F6b, F7a, F7b, and F8 (Singh et al., 2011) from east to west. These features are typically orientated N8°E (Fig. 4e) and show a westward dip component. Sub-bottom 3.5 kHz profiles crossing the faults show vertical offsets of the uppermost sedimentary layers across the fracture zones documenting recent activity (Figs. 3c, S2).

These faults are segmented by en echelon compressional and extensional relays (Figs. 3b), common along strike-slip faults

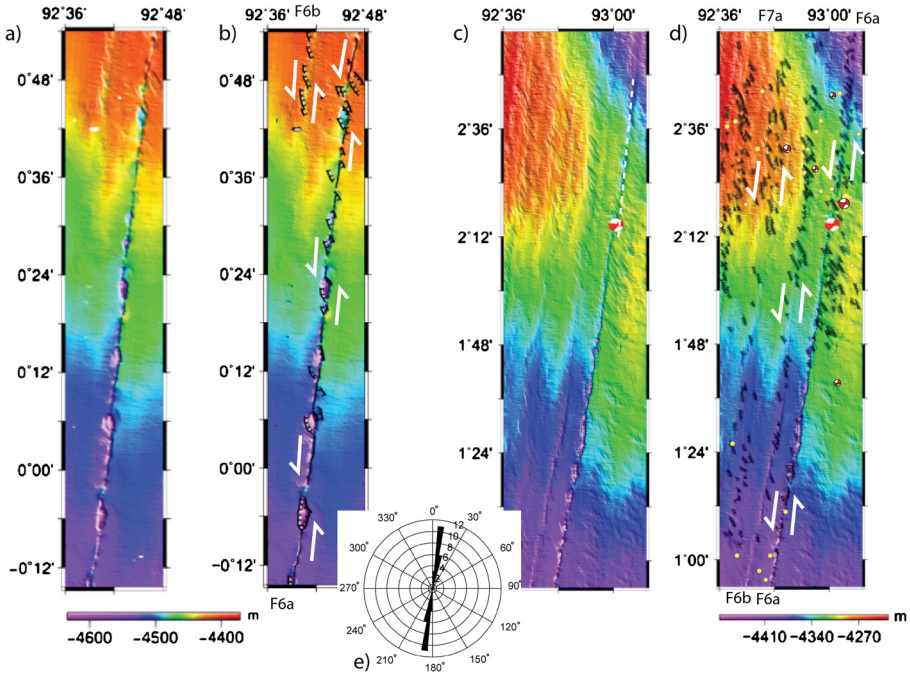


**Fig. 4.** Shaded relief bathymetry and tectonic interpretation of the reactivated fracture zones F6 in its southern segment (panels a and b) and northern segment (panels c and d) (see Fig. 3a for location). The red beach ball represents the focal mechanism of the 2012 main shock. Black solid lines show seafloor faults and white arrows indicate sense of motion (sinistral). White dashed line indicates the location of 3.5 kHz image shown in Fig. S2. Beach balls show historical seismicity in the box. Yellow dots indicate aftershocks between 10 January and 6 November 2012. (e) Rose diagram showing the frequency of orientation of reactivated fracture zones (12 samples).

(Peacock and Sanderson, 1995). The shape of the relays indicates left-lateral movement, consistent with the focal mechanism of earthquakes occurring along these features (Fig. 3a).

Fracture zone F6a is the most prominent N–S striking fracture zone, imaged here over a 400 km distance (Fig. 3a). F6a displays a variable surface expression. In the south, it corresponds to a set of pull-apart basins (Figs. 4b), characterized by vertical offsets of 10–80 m with respect to the surrounding seafloor (Fig. 5), and average lengths and widths of around 5 km and 3 km, respectively. These pull-apart basins are formed as a result of transtension across releasing step-overs (Fig. 5). To the north, F6a is expressed by a set of en echelon normal faults (Fig. 4d, Fig. S2). We interpret these structures as tensile cracks that also indicate sinistral motion along the N8 $\pm$ 3°E (Fig. 4e) re-activated faults. It is interesting to note that these normal faults become much more pervasive in the outer rise region, likely due to the effect of plate bending (Fig. S2). The epicenter of the Mw = 8.6 2012 earthquake is located near the F6a fracture zone (Fig. 4c, d), suggesting that the earthquake ruptured fracture zone F6a as its primary N–S to NNE–SSW trending subfault. The epicenter of Mw = 7.2 foreshock is located slightly to the east. Fracture zone F6b runs parallel to F6a at ~12 km further west and dips eastward. This suggests that F6a and F6b may be a conjugate pair of faults, possibly connecting at depth.

Another major re-activated fracture zone can be observed west of F6: fracture zone F7, which shows a complex configuration with two main faults (F7a, F7b). Deformation along these features appears diffuse with a dense network of small and very close en echelon normal faults. In contrast to F6, pull-apart basins are absent along those segments. The epicenter of the Mw = 8.2 earthquake is located on the southern branch of the second segment of this fracture zone (F7b; Fig. 3b), suggesting that the Mw = 8.2 earthquake might have ruptured F7b (Singh et al., 2017). Most of earthquakes in the region lie along the F6–F7 fracture zones (Fig. 3b). Taken together, the F6 and F7 re-activated fracture zones form a major structural boundary.

The new bathymetry data also image a new fracture zone, referred to here as F5b, which had not been previously identified due to the scarcity of marine magnetic anomaly data (Jacob et al., 2014). This fault is expressed by a set of en echelon normal faults in its northern part. In its southern part, deformation is much more intense, with a small extensional basin consisting of small grabens imaged along the fault (Fig. 3b). In the west of our study area, re-activated fracture F8 is encountered, bounding the NER on its east side. The strike of the en echelon normal faults along the fracture zones is 330 $\pm$ 5° (Singh et al., 2017).

Some of these re-activated fracture zones have been identified both further north and south of our study area. Using bathymetry data along with 3.5 kHz profiles, Graindorge et al. (2008) showed that the F6 fracture zone reaches and intersects the deformation front. Carton et al. (2014) have imaged the re-activated F5, F6 and F7 fracture zones on seismic reflection profiles, and showed that some of them have an offset of 300 m at the basement. Singh et al. (2017) have also shown the seismic images of F6 and F7 within the sediments down to the basement at the southern extremity of our study area. Deplus et al. (1998) have also imaged these re-activated fracture zones further south (5°S) of our study area, suggesting that these features extend over a thousand kilometers.

### 3.3. Normal faults

The northeastern part of the surveyed area is characterized by abundant small graben-type features (Fig. S3a) bounded by normal faults (Fig. 6b). They are active and result from extensional bending stresses near the trench. Active normal faults are frequently observed affecting the oceanic plate topography in the vicinity of subduction zone trenches, such as in Central America (Ranero et al., 2003). Such normal faults are induced by the flexure of the oceanic plate outboard of the trench, and they are sometimes accompanied by normal fault earthquake focal mechanisms, such as those observed in Fig. 1b (green beach balls near ~93°E, 3°N). The outer rise faulting may involve the reactivation of the oceanic spreading fabric of the subducting plate if it is favorably oriented (Masson, 1991; Ranero et al., 2003; Grevemeyer et al., 2007). Here the strike of the observed normal

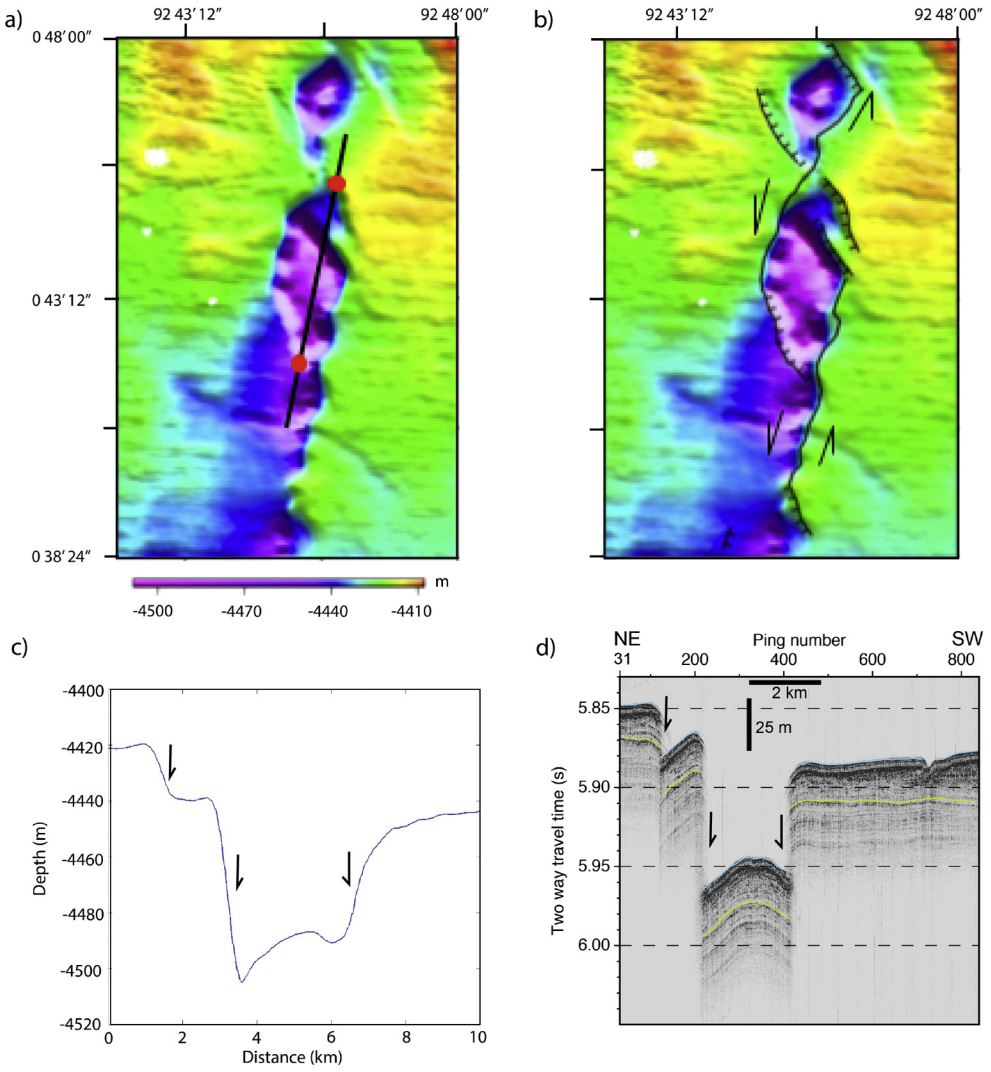


**Fig. 5.** (a) Un-interpreted and (b) interpreted bathymetric image of a pull-part basin along the southern segment of F6a. Black line indicates the location of bathymetry (c) and 3.5 kHz profiles (d). Note the quality and accuracy of 3.5 kHz image. Seafloor is marked in light blue and a sedimentary layer in yellow.

faults (N330°E, Fig. 6e) is more or less parallel to the trench and at an angle to both oceanic fracture zones and abyssal hill normal faults, suggesting that these normal faults are newly formed faults.

In the southeast corner of the surveyed area, N–S oriented graben-type features can be observed (Fig. 6c) south of the newly discovered fracture zone F5b. They are not associated with plate bending, but likely correspond to the southern termination of F5b, causing a wide extensional zone. These normal faults have the same strike, N330°E (Fig. 6e), as that of the normal faults near the subduction front. The dip of these normal faults is 60–70° near the surface.

### 3.4. WNW shear zones

The majority of the study area is cut by a set of right-lateral shear zones (Fig. 7), striking at N290 ± 5°E (Fig. 7c). They appear as series of graben-type features bounded by sets of en echelon normal faults striking at N335 ± 5°E (Fig. 7d). These shear zones are brittle shear zones, since the deformation is concentrated in a narrow fault zone. They represent the dominant style of deformation between the re-activated fracture zones. The area located between the F5b and the F6a fracture zones is particularly affected by several shear zones parallel to each other spaced at 3 to 6 km, distributed unevenly in the northern and in the southern parts. They change slightly their direction in the vicinity of F6a. These shear zones are also pervasive close to the seamount, and cut through the seamount (Fig. 7b), but they are absent northwest of the system of thrust faults. In the northwestern part of the study area, these shear zones again become pervasive.

Toward the western part of the study area (Fig. 3b), the NER is cut by a set of faults, which we interpret as WNW–ESE shear zones, as they are oriented WNW–ESE but also because they are consistent with the observed dominance of strike-slip focal mechanisms for the northern NER earthquakes (Fig. 1b). Sager et al. (2013) have observed similar features further north of our study area.

Singh et al. (2017) discovered these shear zones using only limited data, but our results show that these shears are indeed very prevalent. They suggested that the 2012 great Wharton Basin earthquakes rupture proceeded in en echelon fashion with this suite of N290°E striking shear zones connecting the re-activated fracture zones (F6 and F7), with another N–S trending re-activated fracture zone on the NER. Furthermore, in the southern part of the surveyed area just close to the seamount (between 91°30′E and 92°10′E, Fig. 7b), one of the WNW shear zones seems to be more developed, with a clear fresh trace on the bathymetry, showing a large pull-apart basin manifested by en echelon normal faults and bounded by normal faults (Fig. S4). The shear zone also offsets the

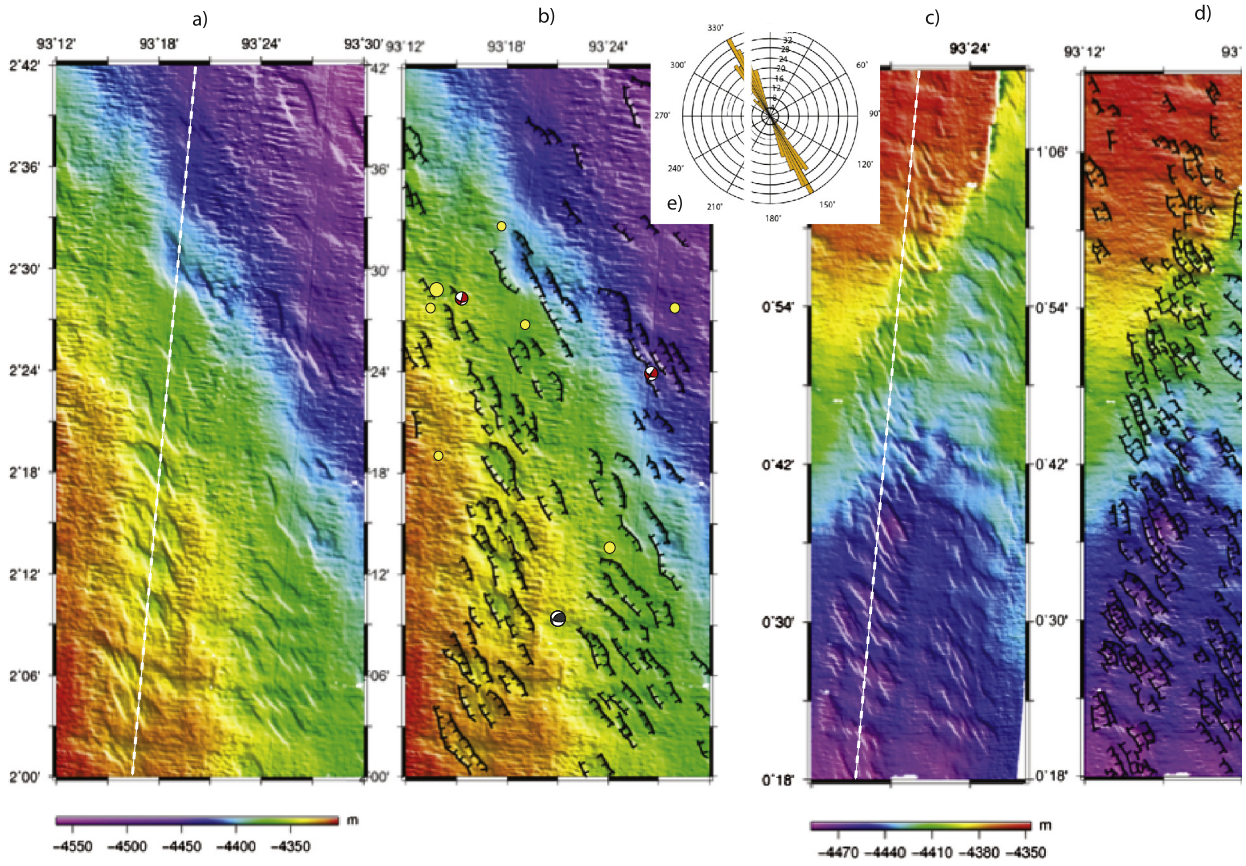


**Fig. 6.** Shaded relief bathymetry map (a) and tectonic interpretation (b) of bending-related normal faults. Beach balls show historical seismicity in the box. Yellow dots indicate aftershocks between 10 January and 6 November 2012. Shaded relief bathymetry map (c) and tectonic interpretation (d) of en echelon normal faults of the southern termination of the F5b reactivated fault (see Fig. 3a for locations). Black solid lines show faults, white arrows indicate F5b. White dashed lines indicate the locations of 3.5 kHz images shown in Figs. S3a (bend faults) and extensional faults (Fig. 3b). (e) Rose diagram showing the orientation of these two systems of normal faults (36 samples).

seamount by approximately 2.5 km (Fig. 7b). Furthermore, the majority of aftershocks are located along this shear zone, suggesting that this area might have ruptured during the 2012 great earthquake sequence, possibly the first direct seafloor evidence confirming the existence of a WNW–ESE component of rupture during the Mw 8.6 event.

### 3.5. NNE shear zones

West of fracture zone F7, particularly at the western corner of the bathymetry map, a series of closely spaced (5 to 10 km) depressions can be observed (Fig. 8a). These depressions correspond to graben-type features, and form long parallel lineaments with a NNE–SSW trend. We interpret these structures as left-lateral shear zones (Fig. 8b) striking at N20 ± 2°E (Fig. 8c). These features are similar to the shear zones described previously and have the same characteristics as the trend of en echelon faults bounding the small depressions (N335°E) (Fig. 8d). Furthermore, in the northwestern corner (~92°E), they intersect the WNW–ESE trending shear zones and the reactivated fracture zones (at ~92°30′E) (Fig. 3b). They are present in the vicinity of the re-activated fracture zones (F7 and F8), not in the middle, and have the same sense of motion, suggesting that they are genetically related.

These shear zones are also brittle, since the deformation is concentrated in a narrow region, characterized by closely-spaced faults, numerous graben basins and shear fractures. The small grabens are bounded by en echelon faults; all these en echelon faults show a predominantly normal sense of motion with a vertical offset on the seafloor on the scale of 5 to 10 m, with a strike of 330 ± 5° (Fig. 8d). Using very limited bathymetry data, Geersen et al. (2015) noticed these features, and interpreted them as P Riedel shears. As we shall discuss below, they are not P Riedel shears, instead they are R Riedel shears and are one element of the complex deformation in the Wharton Basin.

### 3.6. Thrust faults

Following the work of Deplus et al. (1998), it has been accepted that the deformation in the Wharton Basin is accommodated mainly by N–S striking re-activated fracture zones. However, a minority of thrust fault mechanisms is recorded in the south of the Wharton Basin (Deplus, 2001), but no evidence of thrust faults was directly observed on the seafloor in the available bathymetric data.

In the central part of our bathymetry map (92°E, 1°30′N), we observe upwarped sediments indicating deformation along thrust faults (Fig. 9). These faults are present mainly in the area located between fracture zones F7 and F8, close to the NER. Their length ranges from 10 km up to 45 km and their dominant orientation is between N60°E and N65°E (Fig. 9d).

They are clearly marked on the bathymetry by high scarps with throw of 15–20 m (Fig. 9c), dipping 30° toward the northwest. Both on the western and eastern sides of these thrusts, one can observe abandoned channels, suggesting that these thrusts are recent. The main active channel lies west of these thrusts (Fig. 3).

Sub-bottom 3.5 kHz profiles crossing these features (Fig. 8c) show hanging walls up-thrust relative to footwalls. Moreover, they affect even the most recently deposited sediments and thus appear to be active. One thrust earthquake is observed west of these thrusts, otherwise the area is devoid of earthquakes (Fig. 9b).

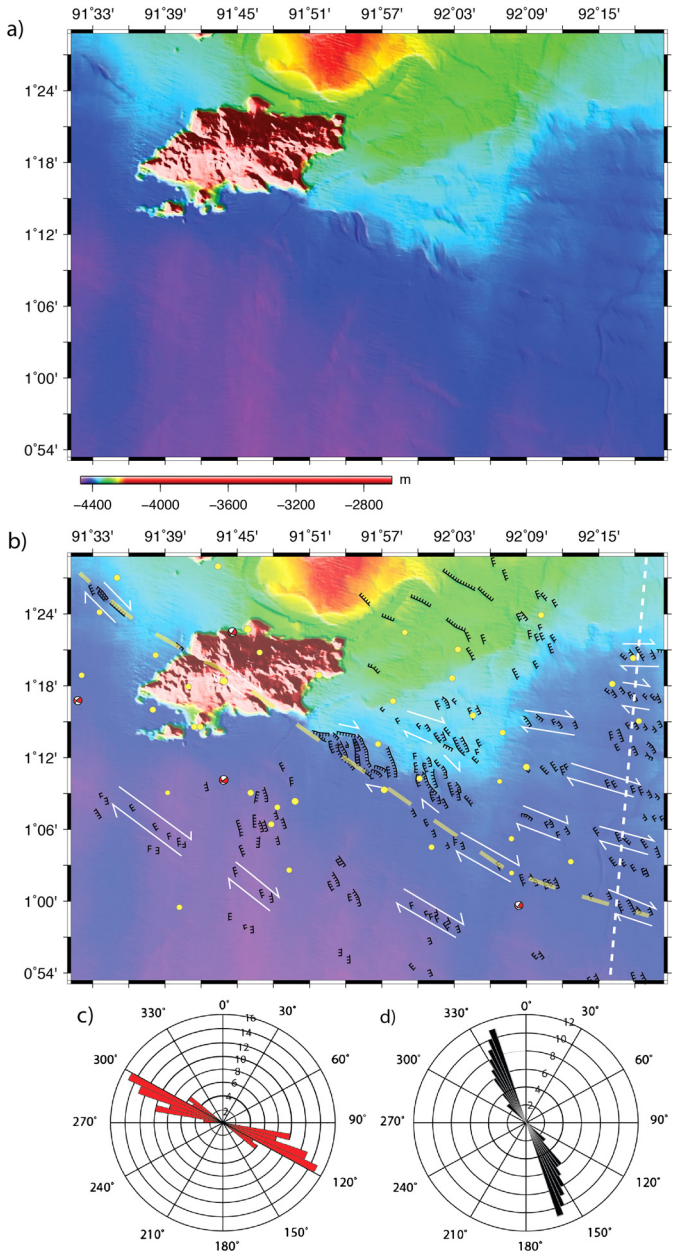


**Fig. 7.** (a) Shaded relief bathymetry map and (b) tectonic interpretation of WNW shear zones (see Fig. 3a for location). Black symbols show normal faults bounding these features and white arrows illustrate sense of motion (dextral). Beach balls show historical seismicity in the box. Yellow dots indicate aftershocks between 10 January and 6 November 2012. Yellow dashed line indicates the possible location of the rupture. (c) and (d) Rose diagrams showing the frequency of orientation of WNW shear zones (16 samples) and related en echelon normal faults (12 samples), respectively. White dashed line indicates the location of 3.5 kHz image shown in Fig. S4.

At the southwestern extremity of this suite of thrusts, there is a 30 km long and 10 km wide seamount, oriented at N75°E, suggesting that there might be a link between the presence of thrust faults and that of this seamount. West of F8, on the NER, there is some evidence of thrusting, with strike similar to the above thrusts. Sager et al. (2013) have noticed upwarping of sediment layers on seismic reflection profiles acquired farther north along the NER, indicating faults with compressional motion, striking at N100°E, less abundant than the WNW–ESE shear zones.

These thrusts are orthogonal to the NW–SE maximum compressive stress direction (Gordon and Houseman, 2015). They may indicate the initiation of folding and buckling of the lithosphere as observed west of the NER.

## 4. Discussion

### 4.1. Link between different types of faulting and regional stress field

Fig. 10 summarizes the orientation of different faults and their link with the local stress directions. Based on the orientations of all these faults, we can define two different stress directions: maximum compressive and maximum extensive stress axes oriented, respectively N335°E and N65°E, orthogonal to each other, with an uncertainty of ±5° (Fig. 10a). Strike-slip faulting occurs in a triaxial stress field in which the maximum and minimum principal stresses $\sigma_1$ and $\sigma_3$ lay in the horizontal plane and the intermediate principal stress $\sigma_2$ is the vertical axis, thus the N335°E oriented compressive stress must be the principal compressional stress $\sigma_1$ and the N65°E oriented extensive stress should be the principal extensional stress $\sigma_3$.

Fig. 10a also suggests that sinistral and dextral faults striking at N20°E and N290°E, respectively, are developed in response to these two main stress axes. These N290°E and N20°E trending shear zones have the same orientation and shear sense (right-handed and left-handed shear senses, respectively) as these two conjugate fault systems (Fig. 10a). Therefore, the N290°E and N20°E shear zones correspond to conjugate structures developed in response to the local stress axes.

It is well known that in the case where an active strike-slip zone lies within an area of continuing sedimentation at low levels of strain, the overall simple shear causes a set of small faults to form. The dominant set, known as R shear, forms at 10–20° to the underlying fault with the same shear sense as the main fault. They often form an en echelon and overstepping array synthetic to the main fault. The R shears are then linked by a second set, the R′ shear, which forms at about 70–80° to the main fault trace (Katz et al., 2004), and these two shears form a conjugate system.

In our case, the strike of the reactivated fracture zones is N8°E, whereas the strike of the NNE–SSW and WNW–ESE trending shear zones is N20°E and N290°E, respectively. The angle between the two sets of shear zones and strike-slip re-activated fracture zones is 12° and 78°, respectively. Consequently, we interpret NNE–SSW shear zones as R Riedel shears and WNW–ESE shear zones as R′ Riedel shears. These two sets of shear zones appear to be formed in response to deformation between the re-activated fracture zones, suggesting that most of the regional-scale deformation is taking place along strike-slip faults.

On the regional scale, the direction and magnitude of maximum compressive and extensional stresses vary from predominantly compressive at the northwest corner to WNW compressive and extensional stresses at the southeast corner of our study area (Fig. 3a). The presence of the Riedel shears and thrusts between the fracture zones F7 and F8 might be due to this regional variation of stresses.

The trend of re-activated fracture zones is oblique to the direction of regional compressive stress; presumably, this mismatch between stress and fault direction could be a result of opportunistic fracturing along major inherited lithospheric discontinuities i.e. fracture zones with large age and crustal thickness contrast. The large-scale regional stresses might be responsible for the re-activation of these fracture zones, whereas the stress field generated between the fracture zones would in turn encourage the development of Riedel shears between the fracture zones (Fig. 10b). Normally Riedel shears are shallow features (Kim et al., 2003) along deep-rooted strike-slip faults. The distance between F7 and F8 is about 170 km, and the Riedel shears seems to extend, in

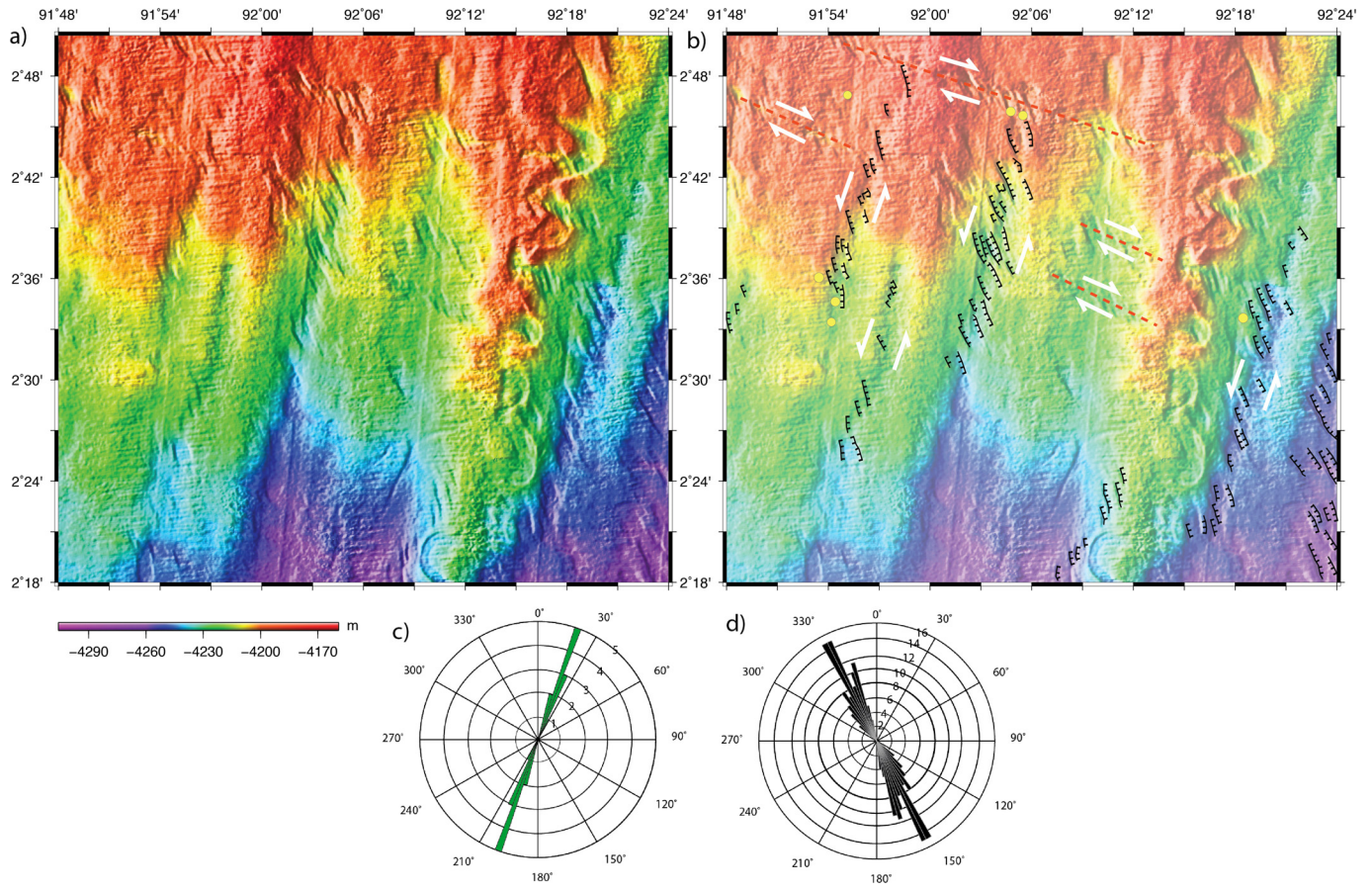


**Fig. 8.** (a) Shaded relief bathymetry map and (b) tectonic interpretation of NNE shear zones (see Fig. 3a for location). Black symbols show normal faults bounding shear zones and white arrows illustrate the sense of motion (sinistral). Red dashed lines and white arrows (dextral sense of motion) mark WNW–ESE shear zones. NNE–SSW shear zones (sinistral sense of motion) are also marked; note that the morphology of these shear zones is similar to that of the WNW–ESE striking shear zones. Yellow dots indicate aftershocks between 10 January and 6 November 2012. (c) and (d) Rose diagrams showing the frequency of orientation of NNE–SSW shear zones (5 samples) and related en echelon normal faults (16 samples), respectively.

an en echelon pattern, for more than hundreds of kilometers, suggesting that these Riedel shears are also deeply rooted on a lithospheric scale.

### 4.2. Shear zones: oceanic fabric reactivation or newly formed structures?

Oceanic fracture zones of the fossil Wharton Spreading Centre are re-activated as left-lateral strike-slip faults in the Wharton Basin; it does not seem to matter that they are oblique to the regional stress pattern. This indicates that deformation has at least partly localized on ancient zones of weakness. Pre-existing structures thus seem to play an important role in the present-day deformation of the Wharton Basin.

By contrast, the N290°E shears strike at an angle of 20–25° with respect to the dominantly E–W oceanic fabric based on the magnetic anomaly pattern (Fig. 3a), and therefore they are likely newly formed. Since no pre-existing NNE–SSW orientation is present in the Wharton Basin oceanic crust, the NNE–SSW shear zones are also newly formed tectonic features.

### 4.3. Thrust faults and existing structures

The observed thrusts have a strike of N60–65°E and the seamount is oriented in a similar direction. The magnetic anomaly data indicate that the strike of the magnetic lineation in this region departs from the general E–W direction and is also N60–65°E, suggesting a local complexity of the Wharton Spreading Centre. The seamount could have been formed during the crustal accretion process or may have developed afterwards; we do not have any constrains on the age of these seamounts. It seems that the observed thrusts have developed along some of these pre-existing volcanic fabrics.

### 4.4. Effect of bending

The re-activated fracture zones and associated shear zones become much more pervasive in the outer rise region of the Sumatran trench; this indicates a complex interaction between the bending stress and the principal compressive stress. The bending stress induces a 200-km wide flexural bulge and a bend towards the subduction front, with abundant extensional deformation and thus an enhanced role of normal faults compared to farther seaward. For example, the re-activated fracture zone F6a is formed by closely spaced en echelon normal faults in the region of the bend (Fig. S2). The strike of normal faults remains the same, i.e. 330–335° azimuths as elsewhere in our survey area.

The bending stresses are generally normal to the subduction direction, which is oblique to the trench in this region. The obliquity leads to a slip partitioning between trench-orthogonal motion along the megathrust and trench-parallel motion accommodated by strike-slip faults in the forearc region (Fitch, 1972). To account for possible rupturing by the 2012 Mw = 8.6 earthquake of a fault segment subparallel to the trench, Ishii et al. (2013) suggested that trench parallel strike-slip faulting due to slip partitioning could also occur in the incoming plate seaward of the trench. However,

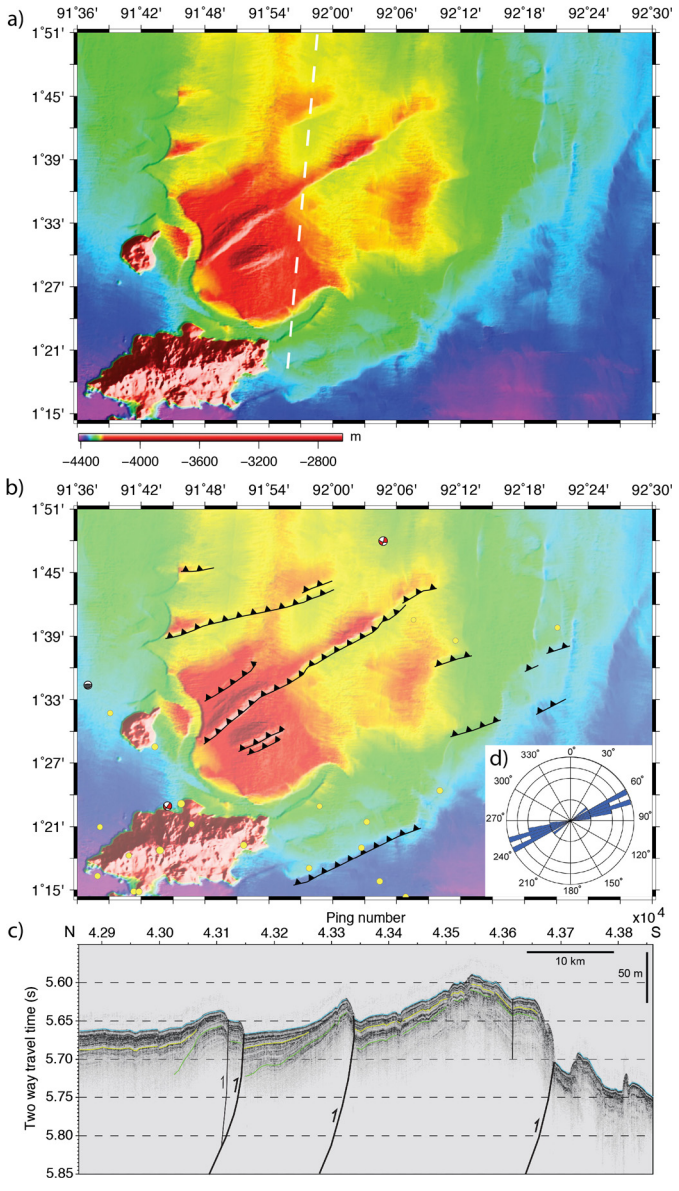


**Fig. 9.** (a) Shaded relief bathymetry map and (b) tectonic interpretation of thrust faults (see Fig. 3a for location). Black symbols show reverse faults. Dashed white line indicates the location of sub-bottom 3.5 kHz profile shown in figure c. Beach balls show historical seismicity in the box. Yellow dots indicate aftershocks between 10 January and 6 November 2012. The black lines indicate thrust faults. (d) Rose diagram showing the frequency of orientation of thrust faults (3 samples).

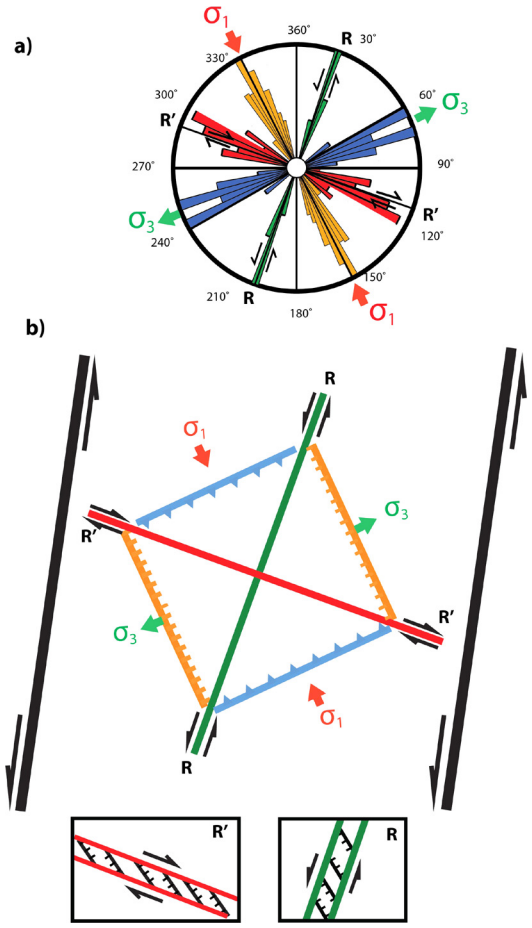


**Fig. 10.** (a) Rose diagram showing the strikes of all normal (orange) and thrust (blue) faults defining the directions of the intra-plate compressive stress $\sigma_1$ (inward pointing red arrows) and the extensive stress $\sigma_3$ (outward-pointing green arrows). The Riedel shears (R and R′) (red: WNW–ESE shear zones, green: NNE–SSW shear zones) indicate the conjugate fault systems, with black arrows indicating the sense of displacement. (b) Schematic diagram summarizing regional and local deformation regime showing all the faults and stresses. Most of the compressive stresses are taken along the re-activated fracture zones and the rest along the shear zones.

the WNW-striking shear zones are very pervasive and extend at least 500 km seaward of the trench, too far for them to be the seaward expression of slip partitioning; these shears are instead caused by the deformation mechanism explained in Fig. 10. On the other hand, as the strikes of bending related normal faults and those forming the WNW shear zones are the same, it is rather difficult to separate the effect of bending-related stress from the regional stress.

### 4.5. Link between the active faulting and the 2012 earthquakes

Many of the 2012 published earthquake models indicate that the Mw 8.6 main-shock involved rupture on multiple NNE–SSW and WNW–ESE trending faults (Ishii et al., 2013; Meng et al., 2012; Yue et al., 2012; Wei et al., 2013), and while the segment showing the largest fraction of seismic moment release was suggested to be either NNE–SSW trending or WNW–ESE trending, our observations of a prominent F6a tend to agree with the former. The Mw = 8.2 aftershock occurred two hours later, rupturing a second NNE–SSW trending fault. Besides the fact that spatial correspondence of earthquakes on oceanic plates with mapped faults is often difficult to ascertain due to location inaccuracies, it is clear that the Mw = 8.6 epicenter aligns along the F6a fracture zone. For the Mw = 8.2, the epicenter aligns along the F7b fracture zone. We suggest that the Mw 8.6 earthquake ruptured several distinct fault segments, starting from the F6a and ending at the F7b. The NNE–SSW shear zones located between the northern and the southern segments of the F7b fracture zone likely linked those segments and transferred rupture along them in en echelon form, and thus, may have hosted some of the moment release during the Mw = 8.6 earthquake. Otherwise, some slip might have occurred along one of these shears. This explains the NE trend component shown by some of the earthquake models (Meng et al., 2012; Wei et al., 2013). Furthermore, the N290°E striking shear zone located close to the seamount is the best candidate for hosting the WNW–ESE rupture (Fig. 7b); the dense pattern of N290°E shear zones in this area strongly suggests high stress drop along several structures in en echelon form. A number of aftershocks also align this shear zone (Fig. 7b). The N290°E shears are present also on the NER, and they likely correspond to the WNW–ESE bathymetric lineations mapped by Sager et al. (2013). We suggest that WNW

shear zones connect the ruptured re-activated fracture zones (F6a and F7b) with another N–S trending re-activated fracture zone on the western side of the NER.

Our findings differ in detail from existing proposed rupture models, due to the fact that the inversion of seismological and geodetic data record can only use long wavelength signals hundreds and thousands of kilometers away from the rupture location. Consequently, these data cannot resolve the slip along each segment separately; instead, they provide an average solution, which to a large extent predict the seafloor observations.

The April 2012 earthquakes have their centroids at 45.6 and 54.7 km depth, respectively (Global CMT Catalog). Furthermore, finite fault models of these earthquakes suggest also rupture down to the base of the lithosphere at a depth of 50 to 60 km (Wei et al., 2013; Yue et al., 2012). Almost the entire depth of the oceanic lithosphere has ruptured. Qin and Singh (2015) have imaged faults down to a depth of 45 km in the northeast of the Wharton Basin, supporting the idea of lithospheric scale faulting during the 2012 earthquake (Wei et al., 2013).

### 4.6. Transition from N–S strike-slip to thrust faulting across the NER

Our bathymetry data show the presence of WNW–ESE shear zones west of the F8, similar to the Wharton Basin. Sager et al. (2013) also observe similar shear zones further west on the NER. The existence of strike-slip earthquakes on the NER suggests that these shear zones are active. Further west of the NER in the Central Indian Basin, west of our study area, most of the earthquakes have strike-slip focal mechanisms (Fig. 1a). Although it has been accepted that the N–S thrusting is a dominant process west of the NER (e.g., Bull and Scrutton, 1992), the presence of the WNW–ESE shear zones on the NER and the large number of strike-slip earthquakes west of the NER suggest that the deformation west of the NER might be similar to the Wharton Basin, more complex than previously realized, and more data are required to answer the real relationship between thrusting and strike-slip faulting.

### 4.7. Time sequence of different faults

The onset of deformation in the Wharton Basin is not well constrained. Using seismic reflection data and assuming an age of 40 Myr for the Nicobar fan sediments, Singh et al. (2017) suggested that the reactivation along the fracture zones started at 17.5 Myr ago. However, the results from IODP drilling site U1480 and U1481 offshore Sumatra indicate that Nicobar fan deposition began 9.5 Myr ago (Hüpers et al., 2017) and shut down at 2 Ma (McNeil et al., 2017), requiring the deformation be much younger. However, as the IODP boreholes lie in the vicinity of the NER and on the bending related flexural bulge, these results may not be applied to the whole Wharton Basin, particularly to the fracture F6a, which is most active.

The sequential development of shear surfaces within a natural Riedel system is difficult to ascertain. Thus, it is difficult to determine the age sequence of different fault systems, but generally speaking, the most widely accepted model for Riedel shear zone development is synthetic driven in the sense that R Riedel shears are normally the first subsidiary fractures to occur and generally build the most prominent set (Bartlett et al., 1981; Katz et al., 2004). But in our case, the WNW shear zones (R′) are more prevalent.

It is well accepted that deformation goes through existing areas of weakness. Since the fracture zones present zones of weakness, stress vectors start first by reactivating them as left-lateral strike-slip fracture zones. As these fracture zones are oblique to principal stress vector (oriented N335°E), deformation created new R Riedel shear zones to accommodate the rest of strain between the re-activated fracture zones. In order to accommodate the rotation of these R shear zones, a second network of R′ Riedel shears oriented WNW–ESE developed. If the relative motion along neighboring fracture zones is different, it could accentuate the development of R′ Riedel shears, and lead to lithospheric scale shear zones. Some of these shear zones extend up to the uplifted area due to thrusting north of the seamount, suggesting that either shear zones are youngest or are the most dominant type of deformation between the fracture zone. However, the presence of inactive channels in this uplifted area indicates that they have migrated westwards, suggesting that these thrust faults are still active. Finally, bending-related faults are the most recently formed, since they are the result of oceanic plate deformation due to the bending just prior to subduction.

## 5. Conclusions

High-resolution multibeam bathymetry, along with sub-bottom profiler data from the source region of the 2012 Wharton Basin earthquake, reveal active processes shaping the seafloor. Based on these new data, the following conclusions can be drawn:

1. Eight re-activated left-lateral N8°E striking fractures (F5b, F6a, F6b, F7a, F7b and F8) are present in the 2012 earthquake rupture zone area. F5b is a newly discovered fracture zone, terminated by an extensional basin at its southern end. Fracture zone F6a appears to be the most active one and has been imaged over a distance of 450 km in the new data; it most likely continues toward the subduction front in the north and extends all the way to the fossil Wharton Spreading Centre in the south (Deplus et al., 1998). This major structure likely ruptured during the 2012 Mw = 8.6 earthquake.

2. Right lateral N290° striking shear zones, present in between the above re-activated fracture zones (including on the NER), are the most pervasive seafloor structures. They are 2–3 km wide, formed by sets of en echelon normal faults, and strike obliquely (at a 20° angle) to the E–W ridge fabric based on magnetic anomalies, suggesting that they are newly formed structures. In the SW part of the survey area, one such prominent shear zone crosses and offsets a large seamount by 2.5 km. This shear zone is the best candidate for an ESE–WNW component of the rupture during the 2012 Mw = 8.6 earthquake.

3. N20°E striking left lateral shear zones are imaged west of fracture zone F7; they appear similar to the N290° striking shear zones but are oriented orthogonal to them. Their strike is in agreement with the strike of one of the nodal planes of the GCMT solution of the Mw = 8.6 event, but it is not clear if they ruptured during the earthquake.

4. En echelon N335° striking normal faults are ubiquitous in the northern Wharton Basin and form key elements for the above three types of strike-slip features. In addition, they also bound an extensional basin south of F5b and accommodate bending related faulting in the north.

5. Thrust faults are imaged between the NER and fracture zone F7 striking N65°E, and their orientation is orthogonal to the maximum direction of compression in the region. These thrust faults are parallel to the local magnetic anomalies, and are bounded in the south by an elongated seamount discovered during the experiment, suggesting that they are associated with pre-existing crustal fabric.

6. The strikes of the normal and thrust faults, orthogonal to each other, define the direction of maximum compressional and extensional stresses in the region, respectively. On the other hand, the N20°E and N290° striking shear zones, also orthogonal to each other, define R and R′ Riedel shears, respectively, which combined with the N8°E re-activated fracture zones explain the whole de-

formation pattern in the region. The stresses localized along reactivated fracture zones, particularly F6a, seem to accommodate most of the N–S component of deformation, with some discontinuous and distributed deformation accommodated by the N20°E striking shear zones. The other component of deformation seems to be distributed along the pervasive N290° striking shear zones, may be recently localized along the WNW shear zone that has produced an offset of 2.5 km.

## Acknowledgements

The data were acquired on board the IPEV R/V Marion Dufresne, under a collaboration between the IPEV, Institut de Physique du Globe de Paris, Earth Observatory of Singapore, and Indonesian Institute of Science. We would to thank Claudio Satriano for providing re-located aftershocks shown in Figs. 4–9. This research is supported by the National Research Foundation Singapore and the Singapore Ministry of Education under the Research Centres of Excellence initiative. This work comprises Earth Observatory of Singapore contribution no. 215 and Institut de Physique du Globe de Paris contribution number 3972.

## Appendix A. Supplementary material

Supplementary material related to this article can be found online at https://doi.org/10.1016/j.epsl.2018.09.007.

## References

Amante, C., Eakins, B.W., 2009. ETOPO1 Global Relief Model Converted to PanMap Layer Format. NOAA-National Geophysical Data Center.

Bartlett, W.L., Friedman, M., Logan, J.M., 1981. Experimental folding and faulting of rocks under confining pressure: part IX. Wrench faults in limestone layers. Tectonophysics 79, 255–277.

Bull, J.M., Scrutton, R.A., 1990. Fault reactivation in the central Indian Ocean and the rheology of oceanic lithosphere. Nature 344, 855–858.

Bull, J.M., Scrutton, R.A., 1992. Seismic reflection images of intraplate deformation, central Indian Ocean, and their tectonic significance. J. Geol. Soc. Lond. 149, 955–966. https://doi.org/10.1144/gsjgs.149.6.0955.

Carton, H., Singh, S.C., Hananto, N.D., Martin, J., Djajadihardja, Y.S., Udrekh, Franke, D., Gaedicke, C., 2014. Deep seismic reflection images of the Wharton Basin oceanic crust and uppermost mantle offshore northern Sumatra: relation with active and past deformation. J. Geophys. Res. 119, 32–51.

Delescluse, M., Chamot-Rooke, N., 2007. Instantaneous deformation and kinematics of the India–Australia plate. Geophys. J. Int. 168, 818–842. https://doi.org/10.1111/j.1365-246X.2006.03181.x.

Delescluse, M., Chamot-Rooke, N., Cattin, R., Fleitout, L., Trubienko, O., Vigny, C., 2012. April 2012 intra-oceanic seismicity off Sumatra boosted by the Banda-Aceh megathrust. Nature 490, 240–244.

Deplus, C., 2001. Indian Ocean actively deforms. Science 292, 1850–1851. https://doi.org/10.1126/science.1061082.

Deplus, C., Diament, M., Hebert, H., Bertrand, G., Dominguez, S., Dubois, J., Malod, J., Patriat, P., Pontoise, B., Sibilla, J.-J., 1998. Direct evidence of active deformation in the eastern Indian oceanic plate. Geology 26, 131–134.

Duputel, Z., Kanamori, H., Tsai, V.C., Rivera, L., Meng, L.S., Ampuero, J.P., Stock, J., 2012. The 2012 Sumatra great earthquake sequence. Earth Planet. Sci. Lett. 351–352, 247–257.

Ekström, G., Nettles, M., Dziewoński, A.M., 2012. The global CMT project 2004–2010: centroid moment tensors for 13,017 earthquakes. Phys. Earth Planet. Inter. 200–201, 1–9. https://doi.org/10.1016/j.pepi.2012.04.002.

Fitch, T.J., 1972. Plate convergence, transcurrent faults, and internal deformation adjacent to Southeast Asia and the western Pacific. J. Geophys. Res. 77 (23), 4432–4460.

Geersen, J., Bull, J.M., McNeill, L.C., Henstock, T.J., Gaedicke, G., Chamot-Rooke, N., Delescluse, M., 2015. Pervasive deformation of an oceanic plate and relationship to large >Mw 8 intraplate earthquakes: the northern Wharton Basin, India Ocean. Geology 43, 359–362.

Gordon, R.G., 2000. Diffuse oceanic plate boundaries: strain rates, vertically averaged rheology, and comparisons with narrow plate boundaries and stable plate interiors. In: Richards, M.A., Gordon, R.G., van der Hilst, R.D. (Eds.), The History and Dynamics of Global Plate Motions. In: Geophysical Monograph, vol. 121. AGU, Washington, DC, pp. 143–159.

Gordon, R.G., Houseman, G.A., 2015. Deformation of Indian Ocean lithosphere: evidence for a highly nonlinear rheological law. J. Geophys. Res. 121, 4434–4449.

Graindorge, D., Klingelhoefer, F., Sibuet, J.-C., McNeill, L., Henstock, T.J., Dean, S., Gutscher, M.-A., Dessa, J.X., Permana, H., Singh, S.C., Leau, H., White, N., Carton, H., Malod, J.A., Rangin, C., Aryawan, K.G., Chauhan, A., Galih, D.R., Greenwood, C.J., Laesanpura, A., Prihantono, J., Royle, G., Shankar, U., 2008. Impact of lower plate structure on upper plate deformation at the NW Sumatran convergent margin from seafloor morphology. Earth Planet. Sci. Lett. 275, 201–210.

Grevemeyer, I., Ranero, C.R., Flueh, E.R., Klaeschen, D., Bialas, J., 2007. Passive and active seismological study of bending-related faulting and mantle serpentinization at the Middle America Trench. Earth Planet. Sci. Lett. 258, 528–542. https://doi.org/10.1016/j.epsl.2007.04.013.

Heine, C., Müller, R.D., 2005. Late Jurassic rifting along the Australian North West Shelf: margin geometry and spreading ridge configuration. Aust. J. Earth Sci.: Int. Geosci. J. Geol. Soc. Aust. 52 (1), 27–39.

Hill, E.M., Yue, H., Barbot, S., Lay, T., Tapponnier, P., Hermawan, I., Hubbard, J., Banerjee, P., Feng, L., Natawidjaja, D., Sieh, K., 2015. The 2012 Mw 8.6 Wharton Basin sequence: a cascade of earthquakes generated by near orthogonal, young, oceanic mantle faults. J. Geophys. Res. 120, 3723–3747.

Hüpers, A., Torres, M.E., Owari, S., McNeill, L.C., Dugan, B., Henstock, T.J., Milliken, K.L., Petronotis, K.E., Backman, J., Bourlange, S., Chemale Jr., F., Chen, W., Colson, T.A., Frederik, M.C.G., Guèrin, G., Hamahashi, M., House, B.M., Jeppson, T.N., Kachovich, S., Kenigsberg, A.R., Kuranaga, M., Kutterolf, S., Mitchison, F.L., Mukoyoshi, H., Nair, N., Pickering, K.T., Pouderoux, H.F.A., Shan, Y., Song, I., Vannucchi, P., Vrolijk, P.J., Yang, T., Zhao, X., 2017. Release of mineral-bound water prior to subduction tied to shallow seismogenic slip off Sumatra. Science 356 (6340), 841–844. https://doi.org/10.1126/science.aal3429.

Ishii, M., Kiser, E., Geist, E.L., 2013. Mw 8.6 Sumatran earthquake of 11 April 2012: rare seaward expression of oblique subduction. Geology 41, 319–322.

Jacob, J., Dyment, J., Yatheesh, V., 2014. Revisiting the structure, age, and evolution of the Wharton Basin to better understand subduction under Indonesia. J. Geophys. Res. 119, 169–190.

Katz, Y., Weinberger, R., Aydin, A., 2004. Geometry and kinematic evolution of Riedel shear structures, Capitol Reef National Park, Utah. J. Struct. Geol. 26, 491e501. https://doi.org/10.1016/j.jsg.2003.08.003.

Kim, Young-Seog, et al., 2003. Mesoscale strike-slip faults and damage zones at Marsalforn, Gozo Island, Malta. J. Struct. Geol. 25, 793–812.

Lay, T., Ye, L., Ammon, C.J., Dunham, A., Koper, K.D., 2016. The 2 March 2016 Wharton Basin Mw 7.8 earthquake: high stress drop north–south strike-slip rupture in the diffuse oceanic deformation zone between the Indian and Australian Plates. Geophys. Res. Lett. 43, 7937–7945. https://doi.org/10.1002/2016GL069931.

Liu, C.-S., Curray, J.R., McDonald, J.M., 1983. New constraints on the tectonic evolution of the eastern Indian Ocean. Earth Planet. Sci. Lett. 65 (2), 331–342.

Masson, D.G., 1991. Fault patterns at outer trench walls. Mar. Geophys. Res. 13, 209–225.

McGuire, J.J., Beroza, G.C., 2012. A rogue earthquake offshore Sumatra. Science 336, 1118–1119.

McNeil, L.C., et al., 2017. Understanding Himalayan erosion and the significance of the Nicobar Fan. Earth Planet. Sci. Lett. 475, 134–142.

Meng, L., Ampuero, J.-P., Stock, J., Duputel, Z., Luo, Y., Tsai, V.C., 2012. Earthquake in a maze: compressional rupture branching during the 2012 Mw 8.6 Sumatra earthquake. Science 337, 724–726.

Moeremans, R., Singh, S.C., McArdle, J., Johansen, K., 2014. Seismic images of structural variations along the deformation front of the Andaman–Sumatra subduction zone: implications for rupture propagation and tsunamigenesis. Earth Planet. Sci. Lett. 386, 75–85.

Molnar, P., Tapponnier, P., 1977. The collision between India and Eurasia. Sci. Am. 236, 30–41.

Peacock, D.C.P., Sanderson, D.J., 1995. Strike-slip relay ramps. J. Struct. Geol. 17, 1351–1361.

Petroy, D.E., Wiens, D.A., 1989. Historical seismicity and implications for diffuse plate convergence in the northeast Indian Ocean. J. Geophys. Res. 94, 12301–12319.

Prawirodirdjo, L., Bock, Y., Genrich, J.F., Puntodewo, S.S.O., Rais, J., Subarya, C., Sutisna, S., 2000. One century of tectonic deformation along the Sumatran fault from triangulation and GPS surveys. J. Geophys. Res. 105, 28,343–28,361.

Qin, Y., Singh, S.C., 2015. Seismic evidence of a two-layer lithospheric deformation in the Indian Ocean. Nat. Commun. 6, 8298.

Ranero, C.R., Phipps Morgan, J., McIntosh, K., Reichert, C., 2003. Bending-related faulting and mantle serpentinization at the Middle America Trench. Nature 425, 367–373.

Royer, J.-Y., Gordon, R.G., 1997. The motion and boundary between the Capricorn and Australian plates. Science 277, 1268–1274. https://doi.org/10.1126/science.277.5330.1268.

Sager, W.W., Bull, J.M., Krishna, K.S., 2013. Active faulting on the Ninetyeast Ridge and its relation to deformation of the Indo-Australian plate. J. Geophys. Res. 118, 4648–4668. https://doi.org/10.1002/jgrb.50319.

Sager, W.W., Fullerton, L.G., Buffler, R.T., Handschumacher, D.W., 1992. Argo Abyssal Plain magnetic lineations revisited: implications for the onset of seafloor spreading and tectonic evolution of the eastern Indian Ocean. In: Proceedings of the Ocean Drilling Program, Scientific Results, vol. 123. College Station, Texas, ODP.

Singh, S.C., Carton, H., Chauhan, A.S., Androvandi, S., Davaille, A., Dyment, J., Cannat, M., Hananto, N.D., 2011. Extremely thin crust in the Indian Ocean possibly resulting from plume–ridge interaction. Geophys. J. Int. 184, 29–42. https://doi.org/10.1111/j.1365-246X.2010.04823.x.

Singh, S.C., Hananto, N., Qin, Y., Leclerc, F., Avianto, P., Tapponnier, P.E., Carton, H., Wei, S., Nugroho, A.B., Gemilang, W.A., Sieh, K., Barbot, S., 2017. The discovery of a conjugate system of faults in the Wharton Basin intra-plate deformation zone. Sci. Adv. 3, e1601689. https://doi.org/10.1126/sciadv.1601689.

Wei, S., Helmberger, D., Avouac, J.-P., 2013. Modeling the 2012 Wharton Basin earthquake off Sumatra; complete lithospheric failure. J. Geophys. Res. 118, 3592–3609.

Weissel, J.K., Anderson, M.S., Geller, C.A., 1980. Deformation of the Indo-Australian plate. Nature 287, 284–291.

Wiens, D.A., Stein, S., 1984. Intraplate seismicity and stresses in young oceanic lithosphere. J. Geophys. Res. 89, 11442–11464.

Wiseman, K., Bürgmann, R., 2012. Stress triggering of the great Indian Ocean strike-slip earthquake in a diffuse plate boundary zone. Geophys. Res. Lett. 39, L22304. https://doi.org/10.1029/2012GL053954.

Yue, H., Lay, T., Koper, K.D., 2012. En echelon and orthogonal fault ruptures of the 11 April 2012 great intraplate earthquakes. Nature 490, 245–249.